In Situ Imaging of Silicalite-1 Surface Growth Reveals the Mechanism of Crystallization

Alexandra I. Lupulescu and Jeffrey D. Rimer*

The growth mechanism of silicalite-1 (MFI zeolite) is juxtaposed between classical models that postulate silica molecules as primary growth units and nonclassical pathways based on the aggregation of metastable silica nanoparticle precursors. Although experimental evidence gathered over the past two decades suggests that precursor attachment is the dominant pathway, direct validation of this hypothesis and the relative roles of molecular and precursor species has remained elusive. We present an in situ study of silicalite-1 crystallization at characteristic synthesis conditions. Using time-resolved atomic force microscopy images, we observed silica precursor attachment to crystal surfaces, followed by concomitant structural rearrangement and three-dimensional growth by accretion of silica molecules. We confirm that silicalite-1 growth occurs via the addition of both silica molecules and precursors, bridging classical and nonclassical mechanisms.

Optimizing the physicochemical properties of zeolites for applications ranging from catalysts for fuel and chemicals production to porous substrates for separations and diagnostics can be leveraged by a molecular-level understanding of crystallization. For more than two decades, silicalite-1 (siliceous ZSM-5) has been a prototype for mechanistic studies of zeolites. Efforts to elucidate the mechanism of growth have predominantly focused on identification of the primary building unit, which is most often presumed to be silica nanoparticles that assemble with remarkably uniform size during tetraethylorthosilicate (TEOS) hydrolysis in aqueous solutions. Nonclassical pathways of crystal nucleation and growth involving the aggregation and attachment of nanoparticles are recognized mechanisms for many biogenic and natural crystals, including iron oxyhydroxide (*1*, *2*), magnetite (*3*), gypsum (*4*), noble metals (*5*, *6*), proteins (*7*), and calcium minerals (*8*–*11*). This is in stark contrast to the classical view of crystallization by spontaneous nucleation and growth from the addition of atoms or molecules—a pathway that is perceived by many to play a marginal role in silicalite-1 crystallization. Although both classical and nonclassical pathways have been proposed for silicalite-1 crystallization, in situ evidence has proven to be elusive because of the challenges associated with time-resolved imaging of surface growth.

Silicalite-1 precursors are nanoparticles with dimensions of 1 to 6 nm (*12*–*14*) that form metastable core-shells, which have a disordered siliceous core and a shell of a physisorbed organic structure-directing agent (OSDA) (*14*). During nucleation, a fraction of nanoparticles grows at the expense of others via Ostwald ripening with simultaneous structural transformations, which lead to partially ordered OSDA-silica primary units (*15*–*17*) with indistinct noncrystalline microstructure. Tsapatsis and co-workers provided evidence that silicalite-1 nucleation occurs by the aggregation and subsequent restructuring of evolved nanoparticles (*17*, *18*). Their studies have also suggested that silicalite-1 growth occurs by precursor attachment, which is a hypothesis gleaned from ex situ transmission electron microscope measurements that identified ~5-nm protrusions on crystal exteriors (*19*). The persistence of precursors in growth solutions throughout silicalite-1 crystallization has led to theories and models postulating their involvement as the primary growth unit (*20*). To a lesser extent, it has been suggested (*21*, *22*) that nanoparticles are metastable species that continually supply soluble silica molecules (i.e., monomers and oligomers) as viable growth units. Only in the final stage of crystallization, when the concentration of precursors is negligible, is molecule addition proposed as the predominant mechanism (*23*, *24*). The schematic in Fig. 1A depicts the landscape of mechanistic pathways that exemplifies both classical and nonclassical theories of silicalite-1 crystallization from molecule addition and nanoparticle attachment, respectively.

We used in situ atomic force microscopy (AFM) to monitor the growth of the (010) face of silicalite-1 crystals under realistic synthesis conditions. Silicalite-1 crystals amenable for AFM measurements were synthesized with large (010) surface area (~30 × 10 μm^2) (*25*) and oriented in the plane of imaging by mounting crystals in epoxy on AFM sample disks. We used a retrofitted AFM liquid sample cell (Asylum Research) equipped with a heating peltier capable of achieving high temperatures (25° to 300°C) and custom-designed components that can withstand caustic solutions (pH 10 to 13). The liquid cell is equipped with inlet/outlet ports (fig. S1) used to supply freshly prepared and degassed growth solution at a rate of 0.2 ml/hour (with a 7-hour residence time). Silicalite-1 growth solutions prepared with TEOS and tetrapropylammonium as the OSDA produced optically transparent solutions for AFM imaging at 80°C and atmospheric pressure.

A mechanical artifact of AFM that needed to be addressed was the lateral drift of the cantilever within the *x*/*y* plane, which results in a progressive temporal shift and eventual loss of the initial imaging area. This phenomenon has proven to be less critical when imaging materials that readily

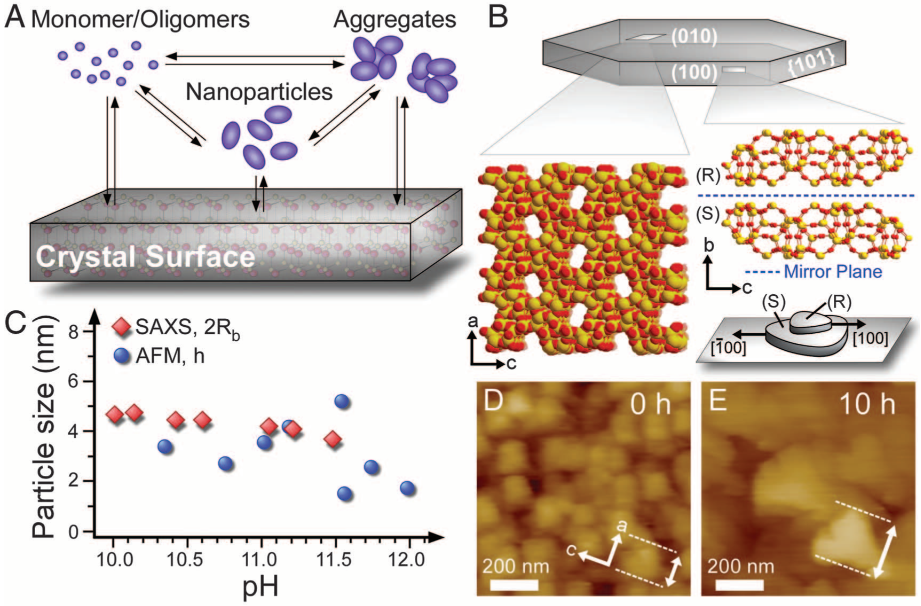

Fig. 1. Precursor attachment to silicalite-1 crystals. (**A**) Pathways of silicalite-1 crystallization. (**B**) Topology of the (010) face, [010] mirror plane, and [100] inversion center of silicalite-1 crystals (MFI type; a = 2.01, b = 1.97, c = 1.31 nm). (**C**) Dimensions of silica precursors from SAXS (minor axis, $2R_b$) and AFM (deposit height, h) after 7 hours at 80°C in growth solutions of pH 10 to 12 (table S1). (**D** and **E**) In situ AFM height mode images reveal the temporal growth of surface features, as indicated by the dashed lines (movie S1).

Department of Chemical and Biomolecular Engineering, University of Houston, 4800 Calhoun Road, Houston, TX 77204–4004, USA.

*Corresponding author. E-mail: jrimer@central.uh.edu

crystallize at ambient conditions (e.g., 25°C), such as biogenic crystals (*26*, *27*), zeotypes (*28*), and select metal-organic frameworks (*29*) in which lower activation barriers for growth unit attachment facilitate rapid time-resolved imaging of surface growth on the order of minutes. High activation energies and concomitant slow rates of zeolite growth necessitate imaging times on the order of hours at high temperatures, which exacerbates lateral drift. To overcome this, we used an AFM scanner with a feedback controller and drift correlation software developed by Asylum Research to achieve small drift rates of ~5 nm/hour, which corresponds to less than 0.3%/hour loss of the imaging area (fig. S2). Analysis of AFM images must also take into account the temporal change in tip geometry due to a gradual deposition of silica that produces a 1.1-nm/hour increase in tip diameter (figs. S3 to S5). Calibration of AFM tips subjected to 20 hours of continuous imaging reveals a less than 2.2% error in height data. As such, mechanistic behavior was evaluated using (010) height data rather than <100> lateral dimensions, which are subject to larger error from tip geometry corrections (~12%, fig. S6) and/or tip artifacts.

We collected AFM images of the (010) face at discrete time points and observed the appearance of deposits with shapes and dimensions resembling those of nanoparticle precursors (Fig. 1, C and D). In order to confirm this, we performed small-angle x-ray scattering (SAXS) on growth solutions to measure precursor size. An oblate ellipsoid form factor provided the best fit of SAXS data (fig. S7 and table S2), in agreement with literature (*14*). We compared ellipsoid *b*-axis ($2R_b$) and *a*-axis ($2R_a$) dimensions from SAXS to those of surface deposits from AFM, measured as the average height *h* (Fig. 1C and fig. S8) and width *w* (fig. S9), respectively. The overlap of nanoparticle and deposit size over a range of growth solution pH provides evidence of nanoparticle attachment to crystal surfaces. Continuous AFM imaging of (010) faces reveals that once adsorbed to the silicalite-1 surface, nanoparticle deposits grow in size (Fig. 1, D and E). In order to minimize the potential dislodgement of deposits caused by the movement of the AFM tip, all images were collected in tapping mode, using a scan rate of 1.4 Hz.

Sequential snapshots of surface growth at 80°C (Fig. 2) show (010) interfaces laden with deposits of nearly uniform size. Terraces on the initial substrate (Fig. 2, A and B) are gradually populated with nanoparticles within the first several hours of heating (Fig. 2, C and D). After 5 hours, the substrate is nearly covered with nanoparticles (Fig. 2, E and F). Continuous imaging was initiated after 7 hours of heating, which equals the liquid residence time in the AFM sample cell (see the supplementary materials for details). Inspection of island height contours, such as line scan $l_{1\text{-}2}$ (Fig. 2E), at various time points reveals three-dimensional (3D) growth. Tracking of individual deposits, such as *d*1 in $l_{1\text{-}2}$ (Fig. 2G), shows a progressive increase in island width, reflecting growth in the <100> directions, and a gradual increase in height along the [010] direction. We recorded several movies that capture the dynamics of island growth. Analysis of successive images from movie S2 reveals that the changes in island dimensions are in increments less than the size of precursors, which is consistent with a mechanism of silica molecule addition. AFM images also reveal processes akin to surface relaxation, which may occur by post-attachment dissolution of precursors and silicate reprecipitation (Ostwald ripening) or by solid-state rearrangement of partially ordered deposits. For instance, the surfaces of *d*1 and nearby deposit *d*2 in Fig. 2G undergo morphological transformations from initially rough to smooth features during growth.

A long-held mechanistic view that growth occurs by the oriented attachment of fully crystalline

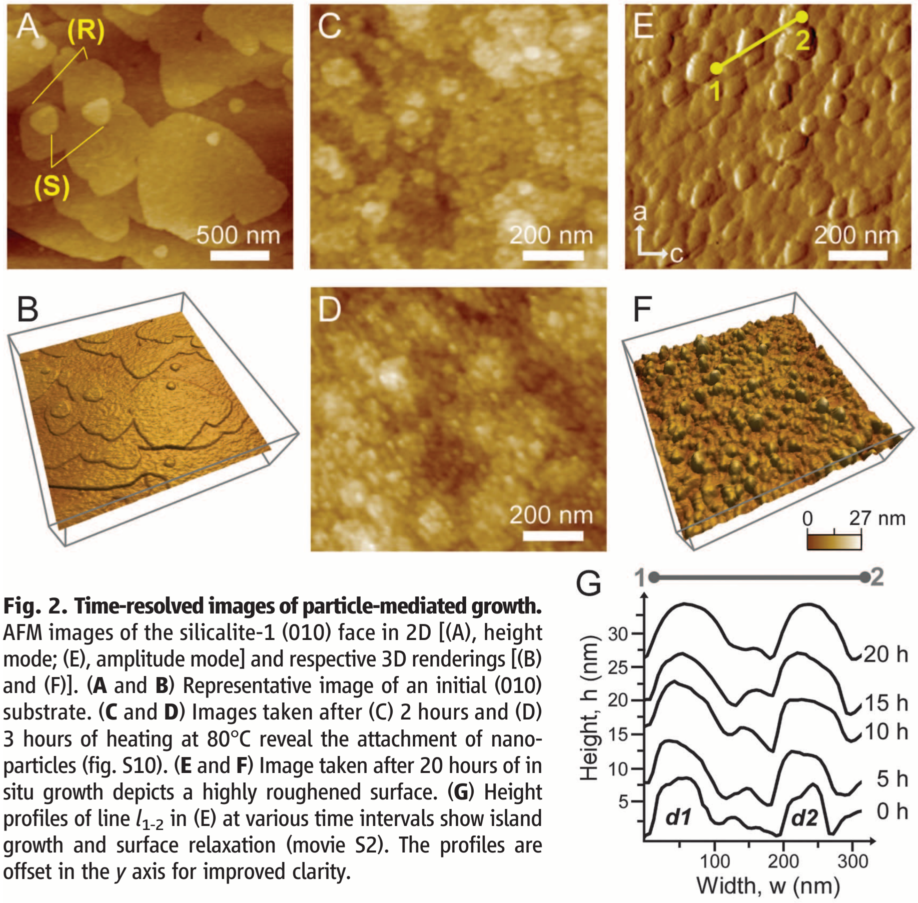

Fig. 2. Time-resolved images of particle-mediated growth. AFM images of the silicalite-1 (010) face in 2D [(A), height mode; (E), amplitude mode] and respective 3D renderings [(B) and (F)]. (**A** and **B**) Representative image of an initial (010) substrate. (**C** and **D**) Images taken after (C) 2 hours and (D) 3 hours of heating at 80°C reveal the attachment of nanoparticles (fig. S10). (**E** and **F**) Image taken after 20 hours of in situ growth depicts a highly roughened surface. (**G**) Height profiles of line $l_{1\text{-}2}$ in (E) at various time intervals show island growth and surface relaxation (movie S2). The profiles are offset in the *y* axis for improved clarity.

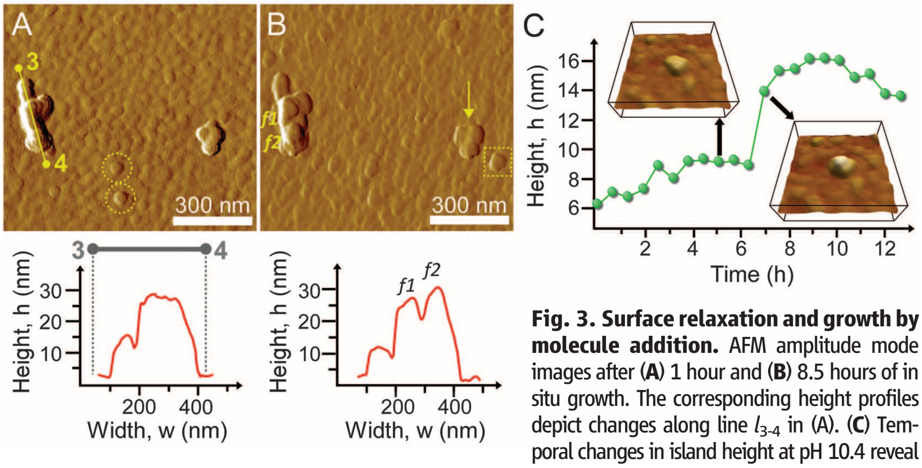

Fig. 3. Surface relaxation and growth by molecule addition. AFM amplitude mode images after (**A**) 1 hour and (**B**) 8.5 hours of in situ growth. The corresponding height profiles depict changes along line $l_{3\text{-}4}$ in (A). (**C**) Temporal changes in island height at pH 10.4 reveal linear growth from silica molecule addition, a step increase around 6 hours from the attachment of a precursor (inset), and decreased height attributed to post-attachment precursor dissolution and/or rearrangement.

precursors (*30*) to silicalite-1 surfaces was supplanted by evidence that precursors are noncrystalline (*15*, *31*); however, pathways involving oriented attachment of partially ordered (evolved) precursor segments can still be envisioned. Moreover, full integration of precursors into the underlying crystal topology necessitates some degree of post-attachment restructuring. Recent studies of minerals have demonstrated multiple pathways for particle-mediated growth, including oriented attachment of crystalline iron oxyhydroxide nanoparticles (*2*) as well as the attachment and rearrangement of disordered nanoparticles in magnetite (*3*). Silicalite-1 disordered-to-ordered surface relaxation is qualitatively consistent with the latter findings; however, if silica precursors align before attachment to the (010) surface, this process is not evident from in situ AFM. Restructuring of disordered deposits may be governed in part by the Ostwald step rule, whereas the creation of highly strained grain boundaries from misaligned precursors would similarly drive particle dissolution or recrystallization, analogous to recent observations by Li *et al.* (*2*). Any loss of translational symmetry during precursor restructuring could lead to crystal defects, such as commonly observed twins, or the misoriented domains detected in aggregates of precursors that become silicalite-1 nuclei (*17*).

Time-resolved images of silicalite-1 crystallization (Fig. 3, A and B) capture the birth, dissolution/rearrangement, and growth of islands. AFM snapshots of surface growth reveal the disappearance of features (Fig. 3A, circles), the emergence of new islands (Fig. 3B, square), and the reduction of feature height due to surface relaxation (Fig. 3B, arrow). For instance, height profiles of line $l_{3\text{-}4}$ (Fig. 3A) depict the partitioning of flattened regions into multiple layers, $f1$ and $f2$ (Fig. 3B). The representative profile tracking the temporal change of island height in Fig. 3C captures all of the dynamic phenomena of silicalite-1 growth. During the first 6 hours of imaging, molecule addition results in a linear increase in height analogous to the [010] growth rate reported in literature (*32*). After 6 hours of growth, there is a step change in height consistent with the attachment of a single nanoparticle precursor. Height mode images (Fig. 3C, inset) show the emergence of a nanoparticle deposit on the island terrace, which is followed by a monotonic decrease in height attributed to post-attachment surface relaxation.

Crystallization mechanisms often involve 2D nucleation and stepwise advancement of layers (Fig. 4A). Anderson and co-workers (*33*) provided evidence of layer growth for silicalite-1 and other zeolites (*32*). Our experiments confirmed that synthesis at 160°C produced faceted silicalite-1 crystals (Fig. 4, B and C) and (010) surfaces composed of steps with heights equal to b/2 (~1 nm) or multiples thereof (Fig. 2A). The MFI crystal structure features a [010] mirror plane (Fig. 1B), where the 180°-reversed orientation of anisotropic islands (Fig. 2A) reflects alternating (*R,S*)-pentasil layers. Earlier ex situ studies of silicalite-1 growth revealed rough (010) faces at high silica supersaturation and the appearance of steps as the concentration of silica approached solubility (*32*). This is consistent with our in situ AFM measurements in supersaturated solutions that reveal surface roughening due to precursor attachment; however, crystallization at 80°C does not yield surfaces with well-defined layers, suggesting a high activation barrier for 2D nucleation and spreading. Silicalite-1 crystallization at low temperature appears to proceed by a 3D mechanism (Fig. 4D and fig. S11). Scanning electron microscopy (SEM) and AFM images collectively confirm that the lower synthesis temperature yields rounded (i.e., nonfaceted) crystals with roughened surfaces (Fig. 4, E and F). Faceted silicalite-1 crystals have previously been observed at low temperature, but after much longer synthesis times (*23*, *24*) via a mechanism that is presumably driven by molecule addition (or Ostwald ripening).

Molecular-level details gleaned from time-resolved in situ AFM measurements provide evidence of silicalite-1 growth by concerted processes that bridge two schools of thought: a classical mechanism based on the addition of silica molecules and a nonclassical route involving the direct attachment of nanoparticles. Although the exact microstructure of precursors and the molecular-level events governing their structural rearrangement have yet to be reconciled, the dynamic processes of silicalite-1 surface growth identified by in situ AFM reveal a complex series of events that transcend conventional mechanisms involving 2D layer nucleation and spreading. The techniques applied here can be extended to a broader class of zeolite structures, and may also prove to be a valuable tool for elucidating the growth mechanism of other materials synthesized by either hydrothermal or solvothermal methods, which include (but are not limited to) metal oxides, minerals, and metal-organic frameworks.

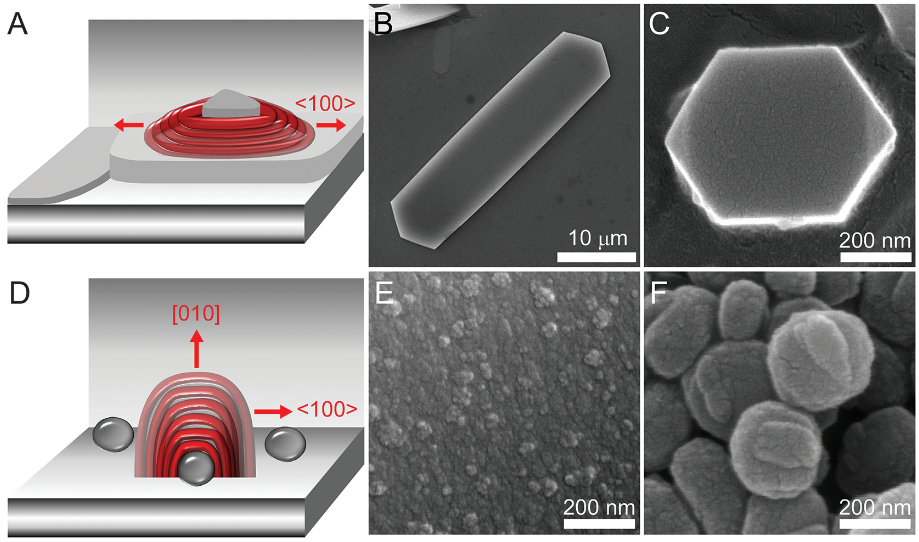

Fig. 4. Different pathways of layered growth. Schematics of 2D layer growth (**A**) and 3D island growth (**D**) depict proposed mechanisms of silicalite-1 crystallization at high and low temperature, respectively. (**B** and **C**) SEM images of faceted silicalite-1 crystals prepared at 160°C using pH 12.7 (B) and 11.4 (C) growth solutions. (**E** and **F**) SEM images of crystals prepared at lower temperature (80°C, pH 11.4) by either seeded (E) or nonseeded (F) crystallization exhibit rough surfaces and spheroidal shapes.

References and Notes

1. J. F. Banfield, S. A. Welch, H. Z. Zhang, T. T. Ebert, R. L. Penn, *Science* **289**, 751–754 (2000).
2. D. S. Li *et al.*, *Science* **336**, 1014–1018 (2012).
3. J. Baumgartner *et al.*, *Nat. Mater.* **12**, 310–314 (2013).
4. A. E. S. Van Driessche *et al.*, *Science* **336**, 69–72 (2012).
5. H. G. Liao, L. K. Cui, S. Whitelam, H. M. Zheng, *Science* **336**, 1011–1014 (2012).
6. H. M. Zheng *et al.*, *Science* **324**, 1309–1312 (2009).
7. S. T. Yau, P. G. Vekilov, *J. Am. Chem. Soc.* **123**, 1080–1089 (2001).
8. D. Gebauer, A. Völkel, H. Cölfen, *Science* **322**, 1819–1822 (2008).
9. W. Habraken *et al.*, *Nat. Commun.* **4**, 1507 (2013).
10. E. M. Pouget *et al.*, *Science* **323**, 1455–1458 (2009).
11. A. F. Wallace *et al.*, *Science* **341**, 885–889 (2013).
12. P. de Moor, T. P. M. Beelen, B. U. Komanschek, O. Diat, R. A. van Santen, *J. Phys. Chem. B* **101**, 11077–11086 (1997).
13. J. N. Watson, L. E. Iton, J. W. White, *Chem. Commun. (Camb.)* **1996**, 2767–2768 (1996).
14. J. M. Fedeyko, J. D. Rimer, R. F. Lobo, D. G. Vlachos, *J. Phys. Chem. B* **108**, 12271–12275 (2004).
15. J. D. Rimer, O. Trofymluk, A. Navrotsky, R. F. Lobo, D. G. Vlachos, *Chem. Mater.* **19**, 4189–4197 (2007).
16. J. D. Rimer, D. G. Vlachos, R. F. Lobo, *J. Phys. Chem. B* **109**, 12762–12771 (2005).
17. T. M. Davis *et al.*, *Nat. Mater.* **5**, 400–408 (2006).
18. S. Kumar, Z. P. Wang, R. L. Penn, M. Tsapatsis, *J. Am. Chem. Soc.* **130**, 17284–17286 (2008).
19. S. Kumar, T. M. Davis, H. Ramanan, R. L. Penn, M. Tsapatsis, *J. Phys. Chem. B* **111**, 3398–3403 (2007).
20. V. Nikolakis, E. Kokkoli, M. Tirrell, M. Tsapatsis, D. G. Vlachos, *Chem. Mater.* **12**, 845–853 (2000).
21. B. J. Schoeman, *Microporous Mesoporous Mater.* **22**, 9–22 (1998).
22. S. L. Burkett, M. E. Davis, *Chem. Mater.* **7**, 920–928 (1995).
23. S. Kumar, R. L. Penn, M. Tsapatsis, *Microporous Mesoporous Mater.* **144**, 74–81 (2011).
24. A. Aerts *et al.*, *Phys. Chem. Chem. Phys.* **13**, 4318–4325 (2011).
25. A. I. Lupulescu, J. D. Rimer, *Angew. Chem. Int. Ed. Engl.* **51**, 3345–3349 (2012).
26. J. D. Rimer *et al.*, *Science* **330**, 337–341 (2010).
27. C. A. Orme *et al.*, *Nature* **411**, 775–779 (2001).

28. M. A. Holden, P. Cubillas, M. P. Attfield, J. T. Gebbie, M. W. Anderson, *J. Am. Chem. Soc.* **134**, 13066–13073 (2012).
29. P. Cubillas, M. W. Anderson, M. P. Attfield, *Chemistry* **19**, 8236–8243 (2013).
30. C. E. A. Kirschhock, R. Ravishankar, P. A. Jacobs, J. A. Martens, *J. Phys. Chem. B* **103**, 11021–11027 (1999).
31. C. T. G. Knight, J. P. Wang, S. D. Kinrade, *Phys. Chem. Chem. Phys.* **8**, 3099–3103 (2006).
32. L. I. Meza *et al.*, *J. Am. Chem. Soc.* **129**, 15192–15201 (2007).
33. M. W. Anderson, J. R. Agger, L. I. Meza, C. B. Chong, C. S. Cundy, *Faraday Discuss.* **136**, 143–156, discussion 213–229 (2007).

Acknowledgments: We acknowledge support from NSF (grants CAREER-1151098 and BRIGE-1032621), the American Chemical Society (grant PRF 52422-DNI5), and the Welch Foundation (grant E-1794). SAXS measurements were performed on an instrument that was purchased with support from NSF (grant MRI-1040446). We are grateful to J. Li and M. Rutgers at Asylum Research for technical assistance.

Supplementary Materials
www.sciencemag.org/content/344/6185/729/suppl/DC1
Materials and Methods
Supplementary Text
Figs. S1 to S11
Tables S1 and S2
References (*34*–*73*)
Movies S1 and S2

17 January 2014; accepted 28 March 2014
10.1126/science.1250984

Recyclable, Strong Thermosets and Organogels via Paraformaldehyde Condensation with Diamines

Jeannette M. García,[1]* Gavin O. Jones,[1] Kumar Virwani,[1] Bryan D. McCloskey,[1,2] Dylan J. Boday,[3] Gijs M. ter Huurne,[4] Hans W. Horn,[1] Daniel J. Coady,[1] Abdulmalik M. Bintaleb,[5] Abdullah M. S. Alabdulrahman,[5] Fares Alsewailem,[5] Hamid A. A. Almegren,[5] James L. Hedrick[1]*

Nitrogen-based thermoset polymers have many industrial applications (for example, in composites), but are difficult to recycle or rework. We report a simple one-pot, low-temperature polycondensation between paraformaldehyde and 4,4′-oxydianiline (ODA) that forms hemiaminal dynamic covalent networks (HDCNs), which can further cyclize at high temperatures, producing poly(hexahydrotriazine)s (PHTs). Both materials are strong thermosetting polymers, and the PHTs exhibited very high Young's moduli (up to ~14.0 gigapascals and up to 20 gigapascals when reinforced with surface-treated carbon nanotubes), excellent solvent resistance, and resistance to environmental stress cracking. However, both HDCNs and PHTs could be digested at low pH (<2) to recover the bisaniline monomers. By simply using different diamine monomers, the HDCN- and PHT-forming reactions afford extremely versatile materials platforms. For example, when poly(ethylene glycol) (PEG) diamine monomers were used to form HDCNs, elastic organogels formed that exhibited self-healing properties.

Nitrogen-containing thermosets, such as poly(amide)s, poly(imide)s, and poly(benzimidazole)s, are used to manufacture adhesives, coatings, foams, automotive and aerospace parts, and electronic devices owing to their high mechanical strength and durability. Despite their widespread commercial use and practical utility, there has been little recent success in the synthesis and design of new high-performance thermosets because of their at-times challenging production. The development of new synthetic platforms that allow for structural modification to impart a variety of useful materials properties, such as high strength or self-healing, is therefore of considerable interest. Furthermore, all known thermosetting polymers are difficult to recycle because they cannot be remolded once cured and thermally decompose upon heating to high temperatures. As a result, a thermoset that can be inherently depolymerized would afford a useful route for thermoset recyclability and redeployment.

We have developed two new related classes of thermosets. The first class, hemiaminal dynamic covalent networks (HDCNs; Fig. 1B, **1.5**) (*1*), was prepared by polymerizing monomers containing two $-NH_2$ units, such as 4,4′-oxydianiline (ODA, **1.4**) or diamine-terminated poly(ethylene glycol) (PEG, **4.2**), with paraformaldehyde at low (~50°C) temperatures. HDCNs exhibited highly versatile properties depending on the diamine monomer used during the polymerization, and properties range from high-strength, chemically robust materials to self-healing organogels that exhibited chemical reversibility in physiological pH regimes. Furthermore, a specific class of HDCNs prepared from ODA underwent a chemical rearrangement when heated to ~200°C and formed the second class of materials, poly(1,3,5-hexahydro-1,3,5-triazines) (PHTs; Fig. 1B, **1.6**), which are highly cross-linked polymer networks.

This work was partially inspired by the synthesis of small-molecule 1,3,5-hexahydro-1,3,5-triazines (HTs; Fig. 1A, **1.3**) (*2*–*7*), which involves the condensation of amines with formaldehyde proceeding through a hemiaminal (HA) intermediate (*8*). To probe the viability of HT formation as a polymer-forming reaction, we studied the trimerization of monofunctional, electron-rich *N,N*-dimethyl-*p*-phenyleneamine with paraformaldehyde as a small-molecule model system by ^{1}H nuclear magnetic resonance (^{1}H NMR) analysis (Fig. 1A). HAs formed within 30 min at 50°C, and at 185°C, the corresponding HT was cleanly synthesized (>98% conversion) within 10 min in deuterated dimethyl sulfoxide (d_6-DMSO, fig. S14). Thus, ^{1}H NMR analysis confirmed successful conditions for both HA and HT formation in the model system at different temperatures. Motivated by these results, we explored the condensation reaction of the electron-rich bisaniline monomer, ODA, with paraformaldehyde as a possible route to synthesize HDCNs and PHTs. Experiments were performed to determine if the reaction between ODA and paraformaldehyde could form the requisite HA intermediate, which could then undergo cyclotrimerization.

The condensation of ODA with paraformaldehyde in *N*-methyl pyrrolidone (NMP, 50°C for 30 min) yielded an intractable polymer powder that was characterized by solid-state ^{13}C NMR. Signals corresponding to aliphatic and aromatic carbons were consistent with reported values for HT, but line broadening inherent in the method made it difficult to differentiate between HDCN and PHT polymers (figs. S3 and S4). Thus, we performed solid-state infrared (IR) measurements on the polymer film after casting at 50°C (Fig. 1C). The sharp signal representative of the NH_2 stretch in ODA was no longer present after heating (fig. S12), and a new set of C−H IR stretching frequencies had been generated, indicative of sp^{3}-hybridized methylene groups incorporated into the structure. In addition to these expected changes in IR signals, a broad signal at ~3300 cm^{-1}, characteristic of an OH stretching signal expected for an HDCN, was measured. Also observed by IR was the carbonyl stretching frequency corresponding to NMP, which presumably remained bound to the polymer (*9*). However, upon ramping the cure temperature to 200°C, the solid-state IR spectrum of the resulting material lacked the broad signal at ~3300 cm^{-1}, suggesting that the OH group was no longer present after heating. In addition, ^{1}H NMR and gel permeation chromatography (GPC) analysis of a soluble polymer was consistent with the construction of an ODA HDCN at 50°C, whereas at 200°C a PHT was formed (fig. S16).

These structural results were supported with calculations using density functional theory (DFT)

---

[1] IBM Almaden Research Center, 650 Harry Road, San Jose, CA 95120, USA. [2] University of California, Berkeley, Department of Chemical and Biomolecular Engineering, 201 Gilman Hall, Berkeley, CA 94720, USA. [3] IBM Tucson, 9000 South Rita Road, Tucson, AZ 85744, USA. [4] Eindhoven University of Technology, Post Office Box 513, 5600 MB Eindhoven, Netherlands. [5] King Abdulaziz City for Science and Technology, Post Office Box 6086, Riyadh 11442, Saudi Arabia.

*Corresponding author. E-mail: hedrick@us.ibm.com (J.L.H.); jmgarcia@us.ibm.com (J.M.G.)

EXTENDED PDF FORMAT
SPONSORED BY

Sample-Size Antibodies
Now Available
Learn More
R&D SYSTEMS
a biotechne brand
www.rndsystems.com

Science AAAS

In Situ Imaging of Silicalite-1 Surface Growth Reveals the Mechanism of Crystallization

Alexandra I. Lupulescu and Jeffrey D. Rimer

Science **344**, 729 (2014);
DOI: 10.1126/science.1250984

This copy is for your personal, non-commercial use only.

If you wish to distribute this article to others, you can order high-quality copies for your colleagues, clients, or customers by clicking here.

Permission to republish or repurpose articles or portions of articles can be obtained by following the guidelines here.

The following resources related to this article are available online at www.sciencemag.org (this information is current as of February 20, 2016):

Updated information and services, including high-resolution figures, can be found in the online version of this article at:
/content/344/6185/729.full.html

Supporting Online Material can be found at:
/content/suppl/2014/05/14/344.6185.729.DC1.html

A list of selected additional articles on the Science Web sites **related to this article** can be found at:
/content/344/6185/729.full.html#related

This article **cites 71 articles**, 15 of which can be accessed free:
/content/344/6185/729.full.html#ref-list-1

This article has been **cited by** 4 articles hosted by HighWire Press; see:
/content/344/6185/729.full.html#related-urls

This article appears in the following **subject collections:**
Materials Science
/cgi/collection/mat_sci

Downloaded from on February 20, 2016

Science (print ISSN 0036-8075; online ISSN 1095-9203) is published weekly, except the last week in December, by the American Association for the Advancement of Science, 1200 New York Avenue NW, Washington, DC 20005. Copyright 2014 by the American Association for the Advancement of Science; all rights reserved. The title *Science* is a registered trademark of AAAS.